Electrochimica Acta 200 (2016) 189–196

Contents lists available at ScienceDirect

Electrochimica Acta

journal homepage: www.elsevier.com/locate/electacta

Localized corrosion of laser marked M340 martensitic stainless steel for biomedical applications studied by the scanning vibrating electrode technique under polarization

Sara M. Manhabosco[a], Álvaro Pritzel dos Santos[a], Marcelo L. Marcolin[a], Eurico F. Pieretti[b], Mauricio D.M. Neves[b], Luís F.P. Dick[a,*,1]

[a] Laboratório de Processos Eletroquímicos e Corrosão, Universidade Federal do Rio Grande do Sul, Av. Bento Gonçalves 9500, Prédio 75, CEP: 91501-970, Porto Alegre, Brazil
[b] Instituto de Pesquisas Energéticas e Nucleares-IPEN/CNEN, Av. Prof. Lineu Prestes, 2242, 05508-000-São Paulo, Brazil

ARTICLE INFO

Article history:
Received 20 November 2015
Received in revised form 27 March 2016
Accepted 29 March 2016
Available online 30 March 2016

Keywords:
Martensitic steel
M340
SVET under polarization
laser marking
pitting

ABSTRACT

The corrosion of laser marked M340 martensitic stainless steel for biomedical applications was investigated using the scanning vibrating electrode technique (SVET) under simultaneous polarization and cyclic voltammetry in a 0.1 M NaCl solution. The laser marking greatly increases the active dissolution of the affected region and decreases the pitting potential due to Cr loss by volatilization and oxidation on the laser-melted zone. Laser marking also increases cathodic currents on the formed oxide resulting in a higher susceptibility to active dissolution and pitting corrosion.

1. Introduction

Cutting devices and other surgical tools require elevated hardness and wear resistance that can be provided by special martensitic stainless steels (SS). Furthermore, biomedical applications require good corrosion resistance to body fluids and cleaning substances. The M340 martensitic SS was originally developed around 2000 by *Böhler Edelstahl GmbH*, Austria, as plastic mould steel, having a high wear resistance at medium and high temperature and low shape deformation after heat treatments [1]. Besides the usual alloying elements Cr, Ni and Mo, N is added to M340, increasing the resistance to pitting corrosion and wear [2]. Moreover, its high hardness together with good corrosion resistance has led to its increasing use in surgical cutting instruments, replacing other stainless steels with high C and Cr content, such as AISI 440 and 420.

For biomedical applications, M340 has been used as tool steel for bone cutters, drills and saws. Laser marking is often applied on the surface of surgical steels to print part identification numbers and, in the case of dental and bone drills, also to indicate the penetration depth of the cutting tool. Several process parameters of Nd:YAG laser marking, such as pulse frequency, energy density input, focal plane offset, scanning speed and pulse duration were optimized in the last decade to achieve high contrast or intense oxide colours. Qi et al. determined for stainless steels that a maximum mark depth was achieved at 3 kHz [3]. For higher pulse frequencies metal evaporation decreases, while oxide formation, Cr content in the surface region and visual contrast all increase [3,4].

We previously studied the corrosion of laser marked austenitic ASTM F139 SS using the scanning vibrating electrode technique (SVET) [5]. At open circuit potential (OCP) conditions in 0.15 M NaCl, only crevice corrosion and unstable and weak localized dissolution could be verified, and this was attributed to the dissolution of redeposited and rapidly solidified metal drops, caused by laser beam induced metal evaporation. Due to the good corrosion resistance of this steel at OCP, we associated the SVET measurements with the simultaneous polarization of the steel [5]. This procedure was introduced and tested previously on the martensitic CA-15 steel, and a good separation between the

* Corresponding author. Tel.: +55 5133087537.
E-mail addresses: smanhabosco@gmail.com (S.M. Manhabosco), alvaropritzel@yahoo.com.br (Á. Pritzel dos Santos), mdlmarcolin@gmail.com (M.L. Marcolin), efpieretti@usp.br (E.F. Pieretti), mdneves@ipen.br (M.D.M. Neves), lfdick@ufrgs.br (L.F.P. Dick).
[1] ISE member.

http://dx.doi.org/10.1016/j.electacta.2016.03.178
0013-4686/

behaviour of martensitic and retained ferrite could be observed for currents lower than around 30 $\mu A\,cm^{-2}$ [6]. It was shown for this SS steel that laser marking, besides increasing its crevice corrosion susceptibility at OCP, pitting potential (E_{pit}) is also decreased [5,7]. This austenitic steel is used for orthopaedic implants and has a composition similar to that of AISI 316L. The increased susceptibility was attributed to a higher Fe content of the outer oxide film layer and to increased electron donor and acceptor densities in the oxide formed on laser marked surfaces [5]. However, besides a lower Cr content, also Mo and Ni depletion was observed for the surface region affected by the laser beam [5,7].

Martensitic SS should undergo full or partial austenitisation of the structure to allow the hardening process, which limits the maximal addition to the steel of the δ-ferrite-stabilizer element Cr to values close to 12 wt.%. Thus, martensitic stainless steels usually have lower corrosion resistance compared to that of Ni-rich austenitic steels with higher Cr content [8].

The structural modifications introduced by laser marking are similar to those introduced by the more intensively studied laser welding process, differing mostly in the depth and extent of the affected area. There are only a few reports on the influence of laser marks on the enhancement of the corrosion susceptibility of stainless steels, while laser marked martensitic steels have not yet been studied. In this work, we looked at the influence of laser marking on the martensitic M340 SS by voltammetry and SVET under simultaneous polarization.

2. Experimental

The AISI M340 martensitic stainless steel samples (wt. % nominal composition: 0.54 C, 0.26 Si, 0.40 Mn, <0.05 P, 1.10 Mo, 17.30 Cr, 0.18 Ni, 0.10 V, 0.11 Cu, 0.19 N, Fe balance) were provided by *Böhler Edelstahl GmbH*-Austria as rods with the dimensions ø = 6 mm, L = 300 mm. For SVET experiments, flat surfaces are necessary. Therefore, the rods were cut along their longitudinal axis resulting in rectangular surfaces with 6 × 40 mm. Before laser marking, the samples were sequentially sanded with SiC papers up to # 4000 and then polished with 1 μm diamond paste. Marking was carried out under industrial conditions using a pulsed Nd:YAG laser (*Techinifor TS420*) at *Sistema de Implante Nacional,* São Paulo/Brazil with laser power of 70 W at a frequency of 40 kHz, scanning speed of 60 mm s^{-1} and pulse duration around 5 ns. The sample surface was placed at a distance of 239.7 mm from the lens with a focal plane offset of 14 mm with spot size around 100 μm. The surface was sequentially marked writing the numeral "8" with the approximate dimensions of 2.5 × 4.0 mm with a single pass.

To reveal the microstructure, samples were exposed for 3 s to Marble's reagent (4 g CuSO4 + 20 mL conc. HCl + 20 mL deionized water). Surfaces were characterized under an *Olympus BX51* optical microscope (OM) and a *JEOL JSM-5800* scanning electron microscope (SEM) provided with energy dispersive X-ray spectroscopy (EDS).

The corrosion studies were performed in 0.1 M NaCl solution. Cyclic voltammetric curves (CVs) were acquired with a scan rate of 1 mV s^{-1} at 25 °C using a conventional three-electrode cell provided with a Pt grid as the counter electrode. The reference electrode was a Ag/AgCl wire (ø = 1.0 mm, 99.99% Ag, *Sigma Aldrich*) placed directly in the solution, prepared as described before [9]. Before each experiment the 0.1 M NaCl Ag/AgCl electrode was polarized in 0.1 M NaCl and its potential ($E_{Ag/AgCl0.1M}$ = 281 mV vs. SHE) checked against a commercial Ag/AgCl electrode. The potentials in the text, however, are informed against the standard hydrogen electrode (SHE). The chloride solution was deaerated by purging nitrogen for 30 min before each measurement. The

For the determination of localized anodic and cathodic sites, current density maps (***j***-maps) were acquired using SVET in naturally aerated 0.1 M NaCl. For this, a Ø = 10 μm electrode was vibrated at a distance of 50 μm from the sample surface with an amplitude around 2 μm. The ***j***-map acquisitions lasted between 5 (blank surfaces) and 9 min (marked surfaces). Several ***j***-maps were acquired consecutively after different immersion times in the solution, ranging from 0 to 90 min. The distance between two consecutive acquisition points Δx varied from around 80 to 120 μm, depending on the size of the scanned area (blank surfaces:

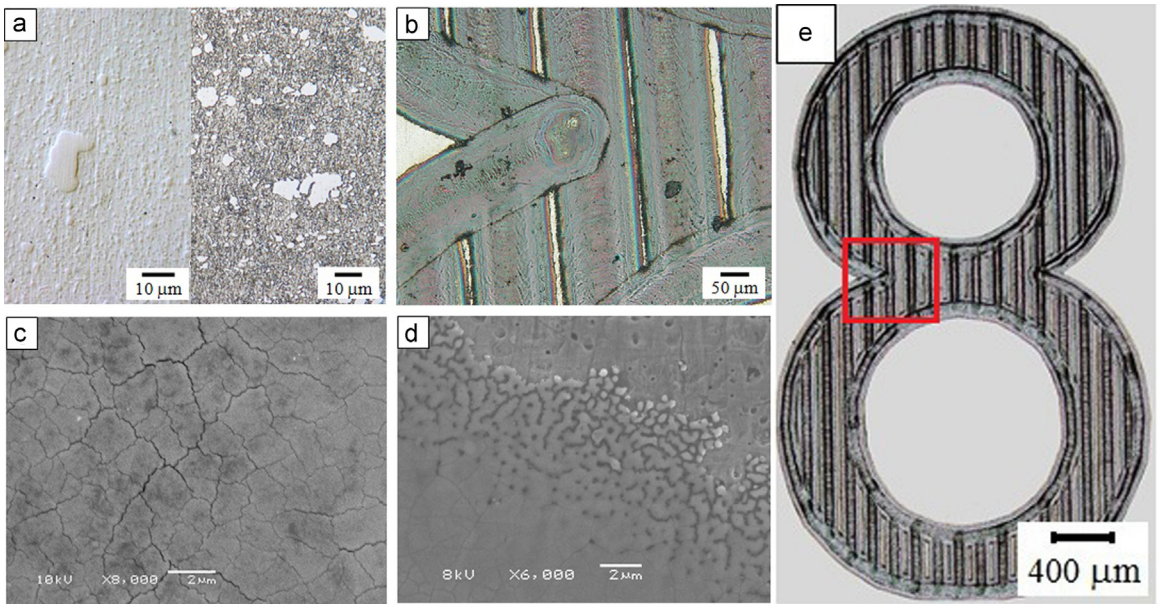

Fig. 1. OM and SEM top view micrographs of M340 SS: (**a**) OM, etched with Marble's reagent, (right) and blank with differential interference contrast (left). (**b**) Top view of laser marked surface (OM detail of **1e**), (**c**) cracked oxide surface (SEM) and (**d**) side edge of melted zone (SEM). (**e**) Low magnification OM view of the laser mark. Red square indicates detail **1b**.

Table 1
Elemental composition ([Me]/∑[Me] × 100at.%) of carbides and M340 matrix.

	Si	V	Cr	Mn	Fe	Mo	N
Carbide 1	0.4	0.5	52.2	0.1	42.8	3.9	n.d.
Carbide 2	0.4	0.6	57.8	0.0	36.4	4.7	n.d.
Matrix 1	0.7	0.0	11.3	0.0	87.3	0.6	n.d.
Matrix 2	0.7	0.2	11.7	0.7	85.9	0.7	n.d.
M340 nominal	0.5	0.1	18.3	0.4	79.3	0.6	0.8

*n.d.: Not detected.

400 points, $\Delta x \approx 80–100\,\mu m$; marked surfaces: 700 points, $\Delta x \approx 120\,\mu m$). ***j***-Maps were also acquired under simultaneous different applied potentials, according to a methodology reported before [5,6]. This procedure is especially appropriate to study the pitting of materials that are more resistant and allows the simultaneous determination of global potentiostatic CVs, which can be then compared to the local current response determined by SVET.

The measuring window exposed to the electrolyte was prepared using scotch tape and carefully delimited with epoxy resin. On laser marked specimens, its size was the same at all electrochemical measurements (SVET, CV and OCP): 2.7×4.16 mm. The mapped area included the whole "8-mark" and was equal to the exposed area. The laser-affected surface comprised approximately 57% of the whole window on these specimens. On blank surfaces, the dimensions of exposed windows were 1.9×2.52 mm or 1.9×1.56 mm for all experiments. The samples were contacted on the backside using a Cu wire and conductive Ag-glue. Due to their small dimension and to avoid contamination of laser marks, instead of embedding in epoxy, sample surfaces were prolonged with scotch tape and then adapted to a cylindrical cell ($Ø \approx 1.5$ cm).

3. Results and Discussion

3.1. OM and SEM-EDS analyses

The M340 stainless steel has a martensitic structure with spheroidized carbides that remain partially undissolved after the final heat treatment of the steel (Fig. 1**a**). On the left side of Fig. 1**a**, the OM view obtained with differential phase contrast shows the carbides in relief. These carbides appear as white particles after attack with Marble's reagent (Fig. 1**a** left, right side) with sizes ranging approximately from 1 to 10 μm. Thus, elements Mo, V and Cr are impoverished in the matrix because of their preferential carbide formation compared to that of Fe, Mn and Si. This is expressed by relative metal content [Me]/∑[Me] × 100 (at.%) determined by EDS analysis for matrix and carbides (Table 1). N was not detected at all due to its low concentration and EDS peak superposition with C at low energies. N is known to increase the passivation and corrosion resistance of stainless steels [8] and consequently may partially compensate the Cr, V and Mo loss of the steel matrix surrounding carbides.

Laser marked patterns on the stainless steel surface are shown in the SEM and OM micrographs of Fig. 1**b**-**d** (top view) and **2** (cross section). The oxidized surface shows interference colours ranging from yellow to blue at the border to a grey tonality on the rest of the laser mark (Fig. 1**b**), indicating that the oxide thickness ranges from around 80 to 150 nm at the colourful side edge, to more than 1 μm at the central part of the laser marked pattern [10]. Cracks are visible on the oxide (Fig. 1**c**), as expected for a thicker thermal oxide. At the side edges of the laser trail, the thinner oxide layer assumes a near dendritic form determined by the retraction of the melt during solidification (Fig. 1**d**). A complete view of the marked are is shown in Fig. 1**e**. The 8-mark is formed by 16 parallel laser tracks and a final pass surrounding the borders of the mark.

The cross section of the marked area (Fig. 2) shows that metal evaporation results in a maximal thickness loss around 2 μm, and the maximal oxide thickness attains approximately 5–10 μm in the centre of the fusion zone (FZ). The findings of other laser processes such as surface welding and laser surface melting may apply to a certain degree to the laser marking process. Metal loss of laser welded steels is explained by the high partial vapour pressures achieved by the metals in the melt pool, due to temperatures exceeding the boiling points of the SS alloying elements [11].

The FZ has a homogeneous fine-grained structure around 10 μm thick (Fig. 2). The cooling rate ($\partial \boldsymbol{T}/\boldsymbol{dt}$) of the FZ reported for laser-melted stainless steels varies from 10^4–10^5 K s^{-1} for the laser surface melting treatment [12], to around 10^3 K s^{-1} for the higher-energy-input process of laser welding [13]. In the laser marking process, the FZ is even thinner than the FZ in the laser surface melting treatment. Therefore, it can be assumed for the laser marking process that metal solidification occurs at an even higher cooling rate than that attributed to the laser surface melting treatment. High cooling rates favour fine grained equiaxial structures and could explain the difficulty of observing dendrites in the FZ of laser marked M340. Moreover, carbide precipitation inside the FZ is also avoided by this high cooling rate. Carbide downsizing also been inferred from X-ray diffraction taken on the surface of femtosecond laser marked martensitic and austenitic stainless steels [14].

Different phenomena occurring during the solidification of the FZ could contribute to compositional changes of laser marked M340, such as element segregation, carbides and nitride dissolution and precipitation, preferential metal volatilization and condensation and selective oxidation. The depth profile of the elemental composition measured on the cross section of the marked steel is listed in Table 2. The points at 1.3, 2.0 and 2.8 μm lie inside the FZ and show that in general the Fe content is enriched in

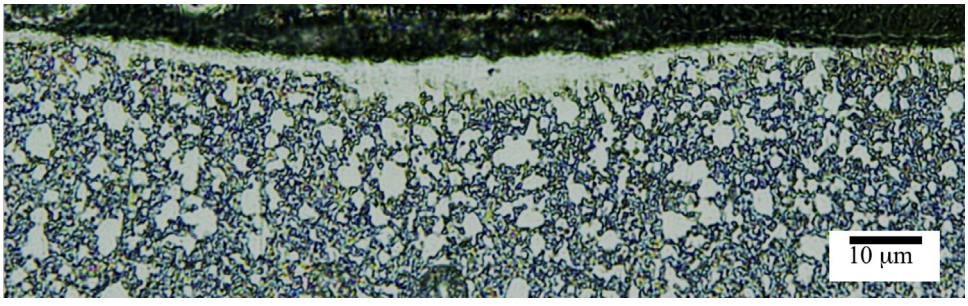

Fig. 2. OM view of cross section of laser marked M340 SS (Marble etching).

Table 2
Elemental composition ([Me]/∑[Me] × 00 at.%) of the laser marked region at different depths from the surface (EDS with electron beam energy of 7 keV).

d/μm*	Si	V	Cr	Mn	Fe	Mo	N
1.30	0.3	0.4	14.0	0.8	83.6	0.9	n.d
2.00	1.3	0.0	14.0	0.6	83.8	0.3	n.d
2.80	1.1	0.0	13.1	0.6	84.9	0.3	n.d
3.60	0.7	0.0	26.2	1.2	70.3	1.6	n.d
4.25	0.2	0.3	57.4	1.3	37.9	2.9	n.d
5.30	0.5	0.0	42.0	1.7	53.7	2.1	n.d

Table 3
Average metallic element composition ([Me]/∑[Me] × 100at.%) ± standard deviation (std. dev.) of the oxide layer formed on the laser melted surface of M340 steel calculated from 10 sampling points at beam energies of 7 and 15 keV.

Beam energy	Si	V	Cr	Mn	Mo	Fe
7 keV	7.6 ± 1.9	2.4 ± 2.9	24.6 ± 14.3	2.1 ± 3.4	0.4 ± 0.4	62.9 ± 10.7
15 keV	0.8 ± 0.5	0.0	17.5 ± 0.0	0.9 ± 0.5	0.3 ± 0.4	80.5 ± 0.0

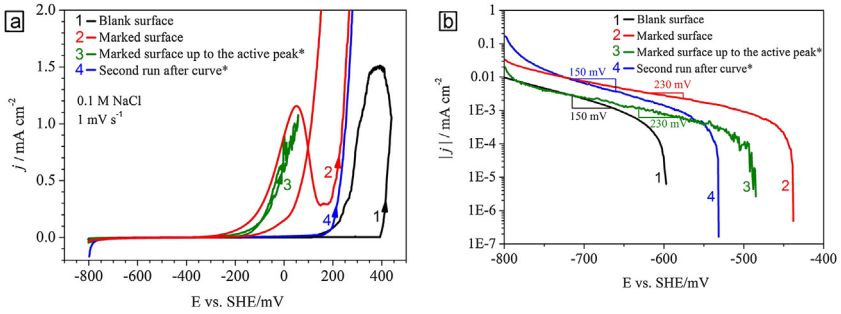

Fig. 3. **a**) CV of M340 SS in 0.1 M NaCl for the blank surface (1-black), marked surface (2-red), marked surface up to the active peak (3-green) and second run after voltametry up to active peak and back (4-blue) (0.1 M NaCl, $\partial E/\partial t = 1$ mV s^{-1}). **b**) Cathodic Tafel slopes the blank surface (1-black), marked surface (2-red), marked surface up to the active peak (3-green) and second run after voltametry up to active peak and back (4-blue). (For interpretation of the references to colour in this figure legend, the reader is referred to the web version of this article.)

the FZ at the expense of the Cr content. The surface region (1.3 μm) additionally shows a lower Si content (Table 2) compared to the nominal composition (Table 1). At greater depths from the marked surface, the composition varies due to the presence of carbides. Compositional changes in the FZ of laser processes are controversial, but a lower Mn is normally cited. According to simulations of laser welding by Sabbaghzadeh et al. [15], Mn and Cr concentrations should decrease within the weld metal, while those of Fe and Ni increase, due to the higher equilibrium vapour pressure of Mn and Cr compared to that of Fe and Ni at high temperatures [13]. Experimental measurements on laser melted austenitic stainless steels with a higher Mn content, such as AISI 201 and AISI 202, [11,16] and on Ni-containing AISI 304L [12] indicated only Mn loss. On the other hand, in the FZ of laser welded high-Ni alloy Haynes 282, Cr and Mo loss were observed, while for femtosecond laser marked martensitic Z30C13 and austenitic 316L SS no compositional changes could be observed [14], most probably due to the very low energy input. A minor surface loss of N due to laser welding was also reported for 201 and 202 SS [16].

Laser marking is usually carried out in the absence of shield-gas. Thus, elements segregated to the liquid are partially lost to the thick thermal oxide formed over the heated metal by selective oxidation. The elemental oxide composition of the marked area was measured by EDS on the top surface using two different beam energies of 7 and 15 keV. Accordingly, the depth of the sampled volume can be roughly estimated using Castaing's equation [17] to ≈0.15 and 0.75 μm for the steel and 0.7 and 2.0 μm, respectively for the oxide layer, considering the formation of chromite ($FeCr_2O_4$). The relative contents of the metallic elements of the oxide layer, [*Me*]/∑[*Me*] in at.%, are listed in Table 3, averaged over 10 sampling points. At the outer oxide layer (7 keV) the metal content varies considerably and the standard deviation is higher, while in the inner oxide layer the Me-content is more constant. This is accordance with simulations of metal flow in the gas phase above the laser melt pool, showing that the metal content on the melt pool is not uniform and the evaporation rates change radially over the melt pool. The elements Si, V, Cr and Mn concentrate in the outer oxide layer due to preferential oxidation, while Fe concentrates in the inner one. Low density Si oxide probably floats to the surface while the enrichment in Mn and Cr of the oxide outer layer may be related to its higher evaporation rate and oxidation on surface of the melt pool. Concerning the most important elements responsible for corrosion resistance, it may be concluded that Cr

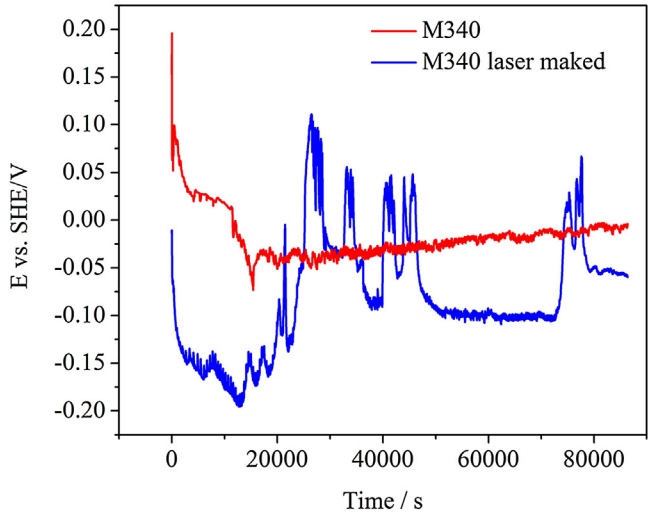

Fig. 4. OCP transients in 0.1 M NaCl of laser marked and blank surface of M340 SS.

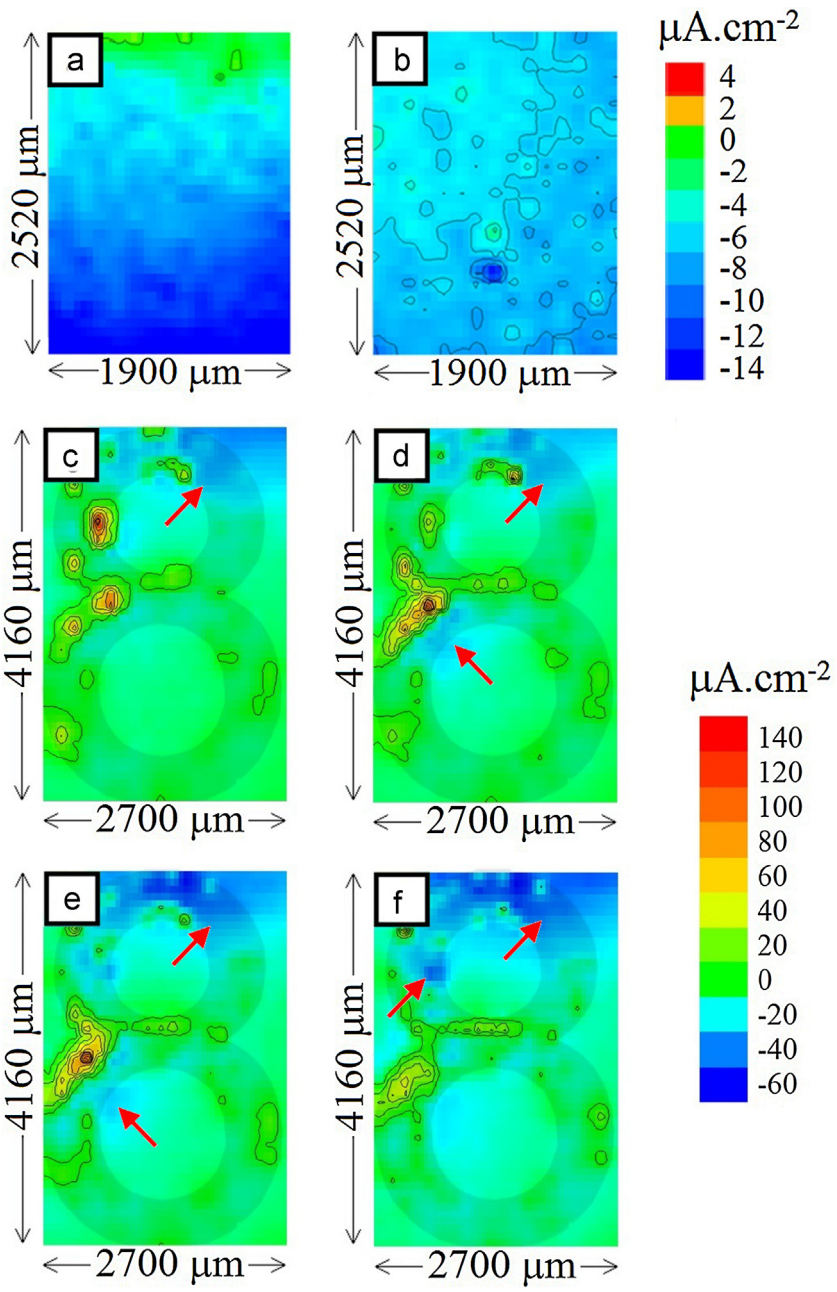

Fig. 5. Time sequence of ***j***-maps obtained from SVET experiments at OCP of (a-b) blank and (c-f) laser marked surfaces of M340 SS in aerated 0.1 M NaCl. Arrows indicate cathodic areas associated to laser marks.

and Si are lost from the metal surface to the oxide layer, while the Mo concentration remains mostly unaffected. Due to the high background at low beam-energies, C and N could not be determined. The formation of Cr_2N is known to occur during welding of stainless steels causing Cr depletion and sensitization similar to that of carbides [15,18,19]. This affects passivity, as Cr and N participate in the passive film formation [19]. However, the fast cooling rate during laser marking avoids sensitization on the surface and the only indication of N loss is that reported in the literature for Mn-N-rich steels [16].

3.2. CV and OCP measurements

Laser marking clearly affects the stainless steel ability to form a stable passive layer, as seen from the voltammograms in Fig. 3**a** comparing blank metal (black, curve 1) and marked surfaces (red, curve 2) and The prominent active peak of the marked surface is completely absent for the blank steel. The pitting occurrence is shifted by the marking process to a lower potential ($\boldsymbol{\Delta E_{pit}}$ = −200 mV), as well as its repassivation ($\boldsymbol{\Delta E_{Rep}}$ = −250 mV). These features are explained by Cr loss within the laser-melted region. If the

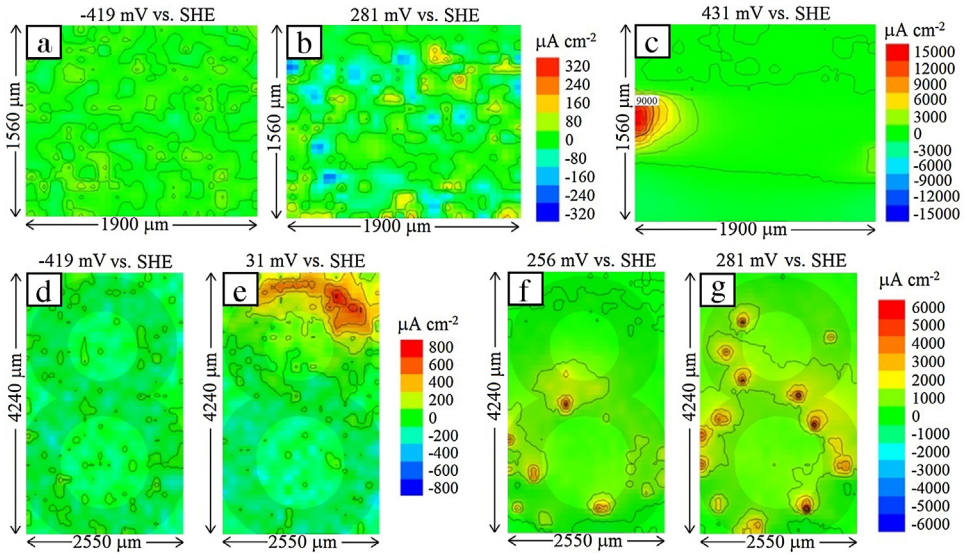

Fig. 6. Potential-sequence of ***j***-maps obtained from SVET experiments under simultaneous polarization of (a-d) (a-c) blank and (e-h) (d-g) laser marked surfaces of M340 SS in aerated 0.1 M NaCl.

polarization on a marked steel surface is reverted within the active peak (green, curve 3) and immediately repeated (blue, curve 4), then the prominent active peak disappears indicating the consumption of a top metal layer with a higher Cr depletion. At the second polarization run, however, pitting still occurs at the same negatively shifted E_{pit} (≈200 mV SHE), as found for the freshly marked surface. The cathodic Tafel slopes of the hydrogen evolution reaction from water $b_c = \partial E/\partial \log j$ determined at polarizations more negative than −80 mV (Fig. 3b) in the absence of O_2 are b_c = 150 mV for the blank surface (black, curve 1) and b_c = 235 mV for the marked steel (red, curve 2 and green, curve 3). At the second polarization run blue, curve 4), the marked surface assumes the same Tafel slope of 150 mV, as that of the blank surface, and ***j*** values of the cathodic reaction increase. This also confirms the dissolution of a top layer with a different composition during the active peak of the marked surface and the removal of the thick and cracked oxide layer on it increasing the exposed area. The thicker cracked oxide at the mark centre is responsible for a less intense cathodic reaction and is partially removed during the dissolution of the laser-melted region. The dissolution penetration depth at the active peak can be calculated from its charge density (198 mC cm^{-2}), obtained form the CV peak area divided by the sweep velocity. Considering uniform dissolution and related data (area fraction marked by laser: 0.569, mean alloy density: 7.7 g cm^{-3}, mean valence: 2.17 electrons/mol, mean molar mass: 55.19 g mol^{-1}), there would be an approximate metal dissolution on the laser mark of only ≈38.6 nm associated with the active peak of the voltammetry, difficult to observe by SEM.

OCP was recorded for longer exposures for samples immersed in aerated 0.1 M NaCl. The OCP value of the blank M340 steel after an initial decay remained in the passive potential range of the steel at −50 mV (SHE) up to 90,000 s. However, for the laser marked steel, OCP was arrested at a potential within that of the active peak for around 20,000 s, when ***E*** oscillations toward +100 mV (SHE) started indicating the onset of pitting after the initial dissolution of the Cr impoverished region (Fig. 4).

3.3. SVET measurements

j-maps were acquired by SVET at OCP on the blank surface (Fig. 5**a**, 0 to 5 min and **b**, 90 to 95 min) and on laser marked steel (Fig. 5**c**, 0 to 9 min, **d**, 30 to 39 min, **e**, 60 to 69 min, and **f**, 90 to 99 min). The maps confirm that the blank steel is not corroded in 0.1 M NaCl (Fig. 5**a**,**b**), as the anodic current densities are bellow the technique sensibility (±2 µA/cm^2) determined on non conductive samples even after 90 min, while the marked steel shows local dissolution with current densities up to 150 µA cm^{-2} after short exposure times (Fig. 5**c**-**f**). The detected localized corrosion spots are clearly positioned within the laser marked area (Fig. 5**c**-**f**). However, after 90 min (Fig. 5**c**), the currents strongly decay, indicating they could be mostly related to the active peak of CV (Fig. 3). It is worth noting that the cathodic areas are also partially associated with the laser marks. These cathodic areas are more clearly seen in Fig. 5**d**, **e** and **f**, respectively, for 30 min, 60 min and 90 min (initial acquisition times). The cathodic areas indicated by arrows cover part of the marked area and are not directly surrounding localized anodic corrosion points. Cathodic ***j*** up to around −60 µA cm^{-2} were determined by SVET (Fig. 5**e** and **f**). Apparently, the oxide layer formed on the laser marked surface is a more efficient cathode for the oxygen reduction reaction and contributes to the corrosion susceptibility of the laser-marked steel.

The respective quasi-stationary voltammograms obtained from the global currents recorded during SVET agree with the facts mentioned above. The Tafel slopes measured from potentiodynamic voltammograms (Fig. 4) are also indicated at the potentiostatic voltammograms of blank (Fig. 7**a**) and marked surfaces (Fig. 7**b**). While the blank surface has a constant Tafel slope compatible with the b_c = 150 mV observed in the potentiodynamic CV's, the apparent b_c value of the marked surface at 25 s changes for times ≥50 s from the respective value observed at the potentiodynamic CV (≈230 mV) to the one observed on blank surfaces. This indicates that the b_c decay of marked surfaces cannot be attributed to the dissolution of a Cr-depleted region, but rather to the modification of the thermal oxide by partial reduction or alkaline attack. The potentiostatic voltammograms of Fig. 7**a**,**b** also allow us to conclude that while on blank surfaces pit nucleation takes between 200 and 300 s at potentials $E > E_{pit}$, on laser marked surfaces pitting nucleates within 25 s.

To verify the pitting distribution on the laser marked areas, SVET experiments were additionally accomplished under simultaneous potentiostatic polarization by applying potential steps of

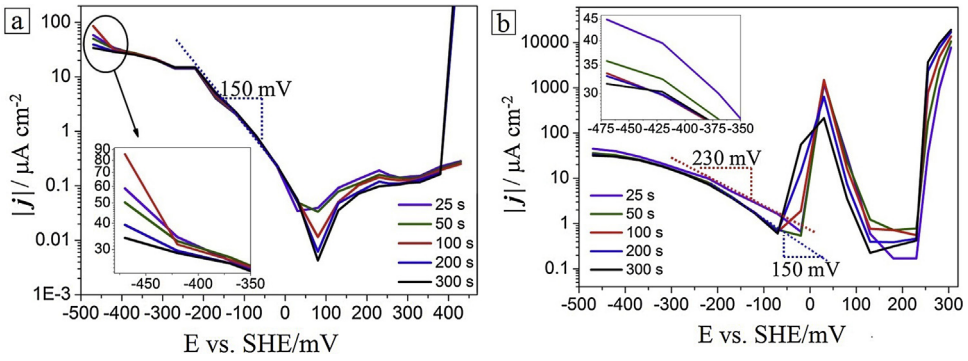

Fig. 7. Quasi-stationary voltammograms determined during SVET mapping under simultaneous polarization for (**a**) blank and (**b**) laser marked surfaces of M340 SS in aerated 0.1 M NaCl.

25 or 50 mV of 9 min each, starting at −470 mV (SHE) toward more positive values. ***j***-maps measured at each applied potential and the global currents were simultaneously acquired. The current maps at selected potentials are presented in Fig. 6**a**-**c** for blank and Fig. 6**d**-**g**, respectively, for laser marked surfaces. The corresponding quasi stationary CVs acquired simultaneously to the SVET maps are shown on Fig. 7. For the blank surface, solely at a more positive potential of 281 mV (SHE), it was possible to see the first anodic

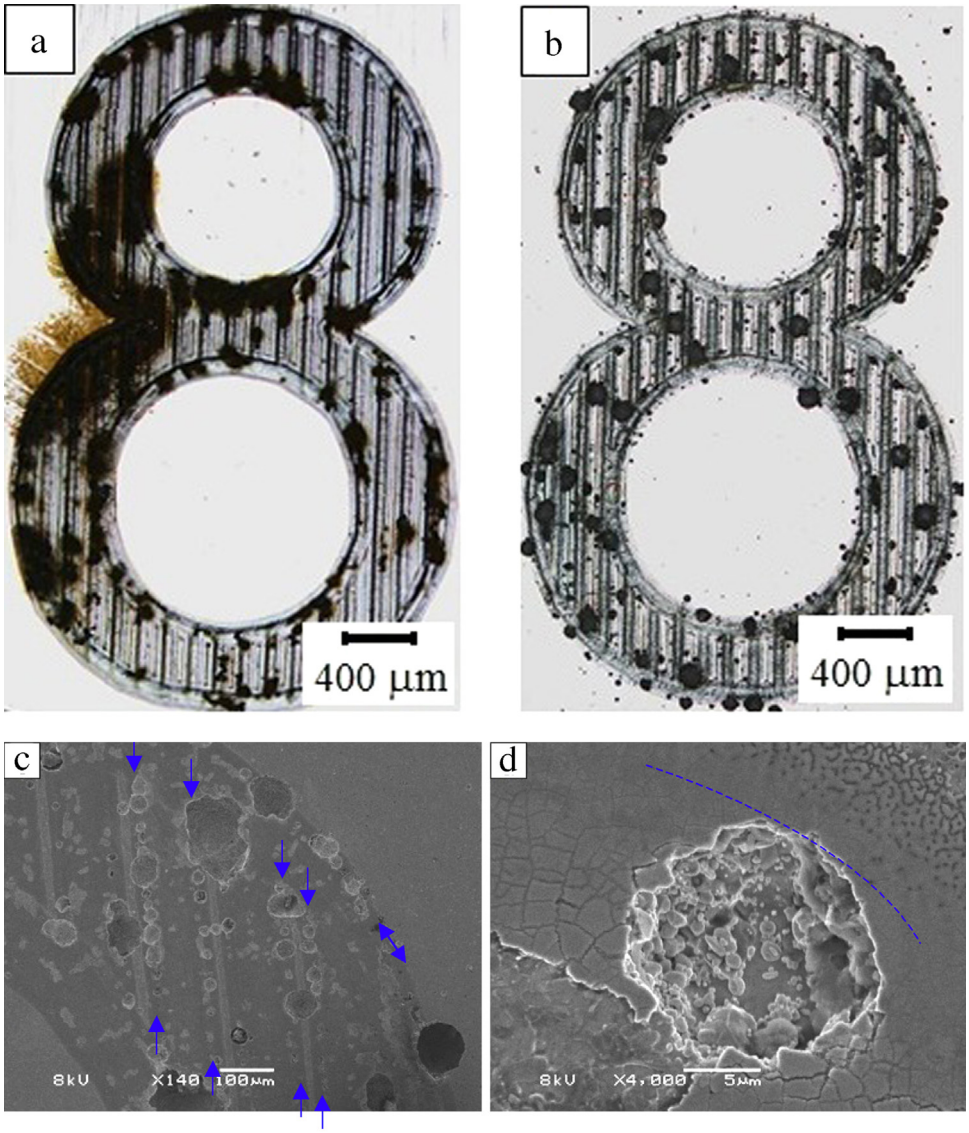

Fig. 8. Low magnification OM view of laser marked M340 SS (a) after exposure for 100 min at OCP conditions and (b) after polarization above the pitting potential (aerated 0.1 M NaCl). (c, d) SEM view of (8.b). Arrows and dashed line indicate the border of fusion zone.

current spots (Fig. 6**b**) and stable pitting at 431 mV (SHE), in accordance with the voltammograms of Fig. 3. However, for the laser marked surface, anodic spots are already visible at potentials above zero (SHE) and pitting at ≈200 mV (SHE), thus in accordance with the potentiodynamic voltammograms. The active dissolution and the pitting spots are clearly associated with the laser marks.

The cathodic areas associated with the laser marks verified before at OCP (Fig. 5**e**-**f**) are no longer visible, when the polarization is started at very negative values. In this case, the surfaces are polarized for 9 min at each potential step before E = OCP is achieved and possible surface modifications are more intense. Preferential cathodic sites may possibly dissolve, or oxide layers are modified by partial reduction or by local alkalinization due to hydrogen evolution, deactivating these sites at potentials bellow OCP.

3.4. Corrosion Morphology

Pits are clearly associated to the laser marks as seen on Fig. 8**a**, **b**. Remarkably, pit nucleation takes place not directly on the centre of the fusion zone, but more frequently at its border (Fig. 8**c**, **d**, arrows and dashed line). Thus, we can possibly associate the observed ***j***-peak with the active dissolution of the Cr depleted zone of the FZ and the preferential pit nucleation site to the heat-affected zone sensitized due to Cr carbides and nitrides precipitation or to Cr segregation outwards and toward the centre of the mark during solidification. The thin phase present at the top of FZ could not be identified, but during the polishing of cross sections, it was observed that this region has a low hardness, indicating the presence of austenite. This would be in accordance with measurements from Conde et al. [20], who at a higher scanning speed during laser surface melting of martensitic 430 SS increasingly observed the formation of austenite. It has been reported that the surface melting process greatly increases E_{pit} and the corrosion resistance of austenitic AISI 310 and 304 SS [20,21] and of ferritic AISI 420 and martensitic 430 SS [20]. Improved corrosion resistance by laser surface melting has been attributed to the replacement of martensite by ferrite and consumption of manganese sulphide inclusions [21] and to the redissolution of carbides and resulting Cr increase in the matrix immediately below the surface [20]. At laser marking, opposite effects to laser surface melting treatment were observed in this study for the martensitic steel, mostly due to the loss of Cr on the fusion zone by preferential oxidation and evaporation as well as sensitization on the mark side edges, which differently than by laser marking are not superimposed by the laser surface scanning procedure.

4. Conclusions

Laser marking enables the active dissolution of the martensitic M340 stainless steel and decreases the pitting potential by around 200 mV and the repassivation potential by 250 mV. Moreover, corrosion susceptibility is increased due to the formation of cathodic preferential sites on the mark as compared to the blank surface.

Laser marking produces Cr-depleted regions mostly due to selective volatilization and oxidation of this element. Besides Cr, also Si is preferentially found in the oxide and their combined depletion may affect the passivity even further.

The active dissolution of the metal was attributed to the dissolution of the central region of the mark trail, where the thermal oxide is thicker, cracked and loose. Pitting however, was observed near the side edges of the laser mark, where sensitization by Cr carbides or nitride precipitation is expected within the heat affected zone or even to the lateral Cr segregation during solidification. Both facts may contribute to a higher pitting susceptibility.

Acknowledgments

The authors acknowledge the *Sistema de Implante Nacional* (SIN) for laser marking specially prepared for this study, the Microscopy Centre of UFRGS for the use of facilities, and CAPES and CNPq for financial support.

References

[1] R. Pierer, R. Schneider, H. Hiebler, Proc. of the 6th International Tooling Conference, Karlstad, Sweden, The behaviour of two new tool steels regarding dimension change, 22002, pp. 611–624.
[2] Y.-S. Yoon, H.-Y. Ha, T.-H. Lee, S. Kim, Comparative study of stress corrosion cracking susceptibility of $Fe_{18}Cr_{10}Mn$ and $Fe_{18}Cr_{10}Mn_1Ni$ based high nitrogen stainless steels, Corrosion Science 88 (2014) 337–348.
[3] J. Qi, K.L. Wang, Y.M. Zhu, A study on the laser marking process of stainless steel, Journal of Materials Processing Technology 139 (2003) 273–276.
[4] Z.L. Li, H.Y. Zheng, K.M. Teh, Y.C. Liu, G.C. Lim, H.L. Seng, N.L. Yakovlev, Analysis of oxide formation induced by UV laser coloration of stainless steel, Applied Surface Science 256 (2009) 1582–1588.
[5] E.F. Pieretti, S.M. Manhabosco, L.F.P. Dick, S. Hinder, I. Costa, Localized corrosion evaluation of the ASTM F139 stainless steel marked by laser using scanning vibrating electrode technique, X-ray photoelectron spectroscopy and Mott-Schottky techniques, Electrochimica Acta 124 (2014) 150–155.
[6] A.P. dos Santos, L.F.P. Dick, Indirect determination of local stationary potentiostatic voltamogramms on CA-15 stainless steel using SVET, 64th Annual Meeting of the International Society of Electrochemistry, Santiago de Queretaro, Mexico, 2013.
[7] E.F. Pieretti, I. Costa, Surface characterisation of ASTM F139 stainless steel marked by laser and mechanical techniques, Electrochimica Acta 114 (2013) 838–843.
[8] A.J. Sedriks, Corrosion of Stainless Steel, 2nd ed., John Wiley & Sons, NY, 1996.
[9] J.C.B. Bertoncello, S.M. Manhabosco, L.F.P. Dick, Corrosion study of the friction stir lap joint of AA7050-T76511 on AA2024-T3 using the scanning vibrating electrode technique, Corrosion Science 94 (2015) 359–363.
[10] J. Enerhaug, Ø. Grong, U.M. Steinsmo, Factors affecting initiation of pitting corrosion in super martensitic stainless steel weldments, Science and Technology of Welding and Joining 6 (2001) 330–338.
[11] K. Mundra, T. Debroy, Toward understanding alloying element vaporization during laser beam welding of stainless steel – A comprehensive model is proposed to predict vaporization rates during welding, Predictions are compared with experimental data, Supplement to the Welding Journal I (1993) 1–9.
[12] O.V. Akgun, O.T. Inal, Laser surface melting and alloying of type 304L stainless steel, Journal of Materials Science 30 (1995) 6097–6104.
[13] L.O. Osoba, R.G. Ding, O.A. Ojo, Microstructural analysis of laser weld fusion zone in Haynes 282 superalloy, Materials Characterization 65 (2012) 93–99.
[14] S. Valette, P. Steyer, L. Richard, B. Forest, C. Donnet, E. Audouard, Influence of femtosecond laser marking on the corrosion resistance of stainless steels, Applied Surface Science 252 (2006) 4696–4701.
[15] M. Jandaghi, P. Parvin, M.J. Torkamany, J. Sabbaghzadeh, Alloying element losses in pulsed Nd:YAG laser welding of stainless steel 316, Journal of Physics. D: Applied Physics 41 (2008) 235503–2355111.
[16] P.A.A. Khan, T. Debroy, S.A. David, Laser beam welding of high-manganese stainless steels – examination of alloying element loss and microstructural changes, Welding Research Supplement to the Welding Journal I (1988) 1–7.
[17] R. Castaing, X-Ray microprobe techniques in X-Ray optics and X-Ray microanalysis, in: H.H. Pattee, V.E. Cosslett, Arne Engström (Eds.), Academic Press, NY, 1963, pp. 263–277.
[18] J.W. Simmons, D.G. Atteridge, J.C. Rawers, Sensitization of high-nitrogen austenitic stainless steels by dichromium nitride precipitation, Corrosion 50 (1994) 491–501.
[19] C.R. Clayton, in: Philippe Marcus (Ed.), Corrosion mechanisms in theory and practice in 'passivity of austenitic stainless steel, 3rd ed., CRC Press, 2002, pp. 327–346.
[20] A. Conde, R. Colaço, R. Vilar, J. de Damborenea, Corrosion behaviour of steels after laser surface melting, Materials and Design 21 (2000) 441–445.
[21] W. Pacquentin, N. Caron, R. Oltra, Effect of microstructure and chemical composition on localized corrosion resistance of a AISI 304L stainless steel after nanopulsed-laser surface melting, Applied Surface Science 356 (2015) 561–573.